

MASTER COPY

KEEP THIS COPY FOR REPRODUCTION PURPOSES

REPORT DOCUMENTATION PAGE			Form Approved OMB No. 0704-0188	
Public reporting burden for this collection of information is estimated to average 1 hour per response, including the time for reviewing instructions, searching existing data sources, gathering and maintaining the data needed, and completing and reviewing the collection of information. Send comments regarding this burden estimate or any other aspect of this collection of information, including suggestions for reducing this burden, to Washington Headquarters Services, Directorate for Information Operations and Reports, 1215 Jefferson Davis Highway, Suite 1204, Arlington, VA 22202-4302, and to the Office of Management and Budget, Paperwork Reduction Project (0704-0188), Washington, DC 20503.				
1. AGENCY USE ONLY (Leave blank)		2. REPORT DATE Mar 95		3. REPORT TYPE AND DATES COVERED Final
4. TITLE AND SUBTITLE "Research in Ground-to-Air Microwave Imaging"			5. FUNDING NUMBERS DAAL03-89-K-0066	
6. AUTHOR(S) Prof. Bernard D. Steinberg and Mr. Donald Carlson				
7. PERFORMING ORGANIZATION NAME(S) AND ADDRESS(ES) Valley Forge Research Center The Moore School of Electrical Engineering University of Pennsylvania 200 S. 33rd St., Philadelphia, PA 19104			8. PERFORMING ORGANIZATION REPORT NUMBER UP-VFRC-11-95	
9. SPONSORING/MONITORING AGENCY NAME(S) AND ADDRESS(ES) U.S. Army Research Office P.O. Box 12211 Research Triangle Park, NC 27709-2211			10. SPONSORING/MONITORING AGENCY REPORT NUMBER ARO 25350.15-EL	
11. SUPPLEMENTARY NOTES The views, opinions and/or findings contained in this report are those of the author(s) and should not be construed as an official Department of the Army position, policy, or decision, unless so designated by other documentation.				
12a. DISTRIBUTION/AVAILABILITY STATEMENT Approved for public release; distribution unlimited.			12b. DISTRIBUTION CODE	

ABSTRACT (Maximum 200 words)

Many potential applications exist for high resolution radar such as direction finding, high accuracy tracking, target counting, and high resolution radar imaging. All of these applications require the use of large, thinned, random or periodic antenna arrays. Many uncertainties exist in such large antenna systems. For example, exact element positions are generally not known because of surveying problems or flexing of the large antenna structure. Adaptive beamforming (ABF) is the solution to the unusual design that achieves these objectives. It deduces the errors in the locations of the receivers that are distributed around the airport or on the air frame and automatically compensates for them in the image processing. This year's work concentrated on three tasks. The first was to develop a generalized ABF theory for the class of spatial correlation algorithms. The second was to extend the resolution of a microwave imaging radar to 15 cm, and the third was to study enhanced target detection sensitivity and target recognition.

SUBJECT TERMS

Radar Imaging

15. NUMBER OF PAGES

16. PRICE CODE

17. SECURITY CLASSIFICATION OF REPORT UNCLASSIFIED	18. SECURITY CLASSIFICATION OF THIS PAGE UNCLASSIFIED	19. SECURITY CLASSIFICATION OF ABSTRACT UNCLASSIFIED	20. LIMITATION OF ABSTRACT UL
--	---	--	----------------------------------

NSN 7540-01-280-5500

Standard Form 298 (Rev. 2-89)

Prescribed by ANSI Std. Z39-18

298-102

03-07-95 03:02PM P002 #13

11026

19950327 176

TABLE OF CONTENTS

	page
1. Introduction	1
2. A Generalized Spatial Correlation-based Algorithm for Self-cohering Large Antenna Arrays	2
3. 2-D High Resolution Microwave Imaging of Ground Vehicles with a UWB Radar System	6
Introduction	6
Features of the Program	6
System Design	6
Experiment Program	8
Range/Amplitude Experimental Results	9
Two-dimensional Imaging Program	11
4. Enhanced Target Detection Using Stereoscopic Display Techniques	15
Introduction	15
Experimental Analysis	15
Three-dimensional Perception and Display	16
Potential Applications of 3-D Radar Imaging	18
Conclusions	19
5. Automatic Target Recognition Using Neural Networks for Microwave Imaging Systems: Preliminary Report	21
Objective	21
Introduction	21
Hardware Implementation of the Neural Network Model	24
Result of Preliminary Investigations	24
References	27

For	
RA&I	<input checked="" type="checkbox"/>
AB	<input type="checkbox"/>
iced	<input type="checkbox"/>
on	
Dist.ribution /	
Availability Codes	
Dist	Avail and/or Special
A-1	

1. INTRODUCTION

The small wavelength of optical radiation ($\sim 1/2 \mu\text{m}$) is largely responsible for the high resolution of optical imagery. Even a small lens such as the one in the human eye images very well because it is about 3000 wavelengths in diameter; its resolution, according to the laws of physics, is $1/3000$ radian or about 0.02 deg. Imaging with the long wavelength used in radar (roughly $1\text{-}30$ cm) is much more difficult. Consider a 5-cm imaging radar, for which the wavelength is $100,000$ times longer than its optical counterpart. To achieve the same resolution as the eye the antenna size must be more than 150 meters, which is nearly the length of two football fields. Even more outlandish is the 5 km antenna required to achieve the resolving power of a small, $2''$ optical telescope.

Adaptive beamforming (ABF) is the solution to the unusual design that achieves these objectives. With ABF an air traffic controller's radar could utilize target echoes from several microwave receivers distributed around the airport and deliver high resolution images – not merely the usual radar blips – to a monitor scope. The resolution would be of small-telescope quality, good enough perhaps to see if the wheels were down. The same type of system – called a radio camera – aboard an airplane would provide a passing-scene display, in the cockpit, of the terrain below with resolving power comparable to the human eye. This display would operate in all weather and night and day.

Adaptive signal processing is the means by which ABF enables the radio camera to achieve this extraordinary resolution. It deduces the errors in the locations of the receivers that are distributed around the airport or on the air frame and automatically compensates for them in the image processing. The information is obtained from the echo-wavefront measurements made by the receivers. In short, the system is dynamically self-calibrating.

This year's work concentrated on three tasks. The first was to develop a generalized ABF theory for the class of spatial correlation algorithms. This class is the largest and appears to be the most generally useful. A single, general algorithm has been written that encompasses all known members of the class. When the tolerance theory, currently being developed, is finished, a complete engineering design theory will be available for high resolution imaging radar.

The second task extended the resolution of microwave imaging radar from a 1-meter resolution cell, which is satisfactory for airplane targets, to the 15 cm needed for recognition of ground targets. A 3-band , dual polarization radar was built with 1-GHz bandwidth for this task. Prominent specular echo resonances from sides and floor appear in images of small pick-up trucks at $L\text{-band}$ (10-cm wavelength) while the same sides and floor scatter the incident energy – appear rough – at $K_u\text{-band}$ (1.6 cm). This difference in the backscattering characteristics enhances the target recognition potential when images from different frequency bands are combined.

Enhanced target detection sensitivity and target recognition was the third thrust. We improved detection sensitivity by the order of 20 dB – a factor of 100 – with an electronic 3-D display of our high resolution microwave images of aircraft. We also learned that simple neural networks can recognize the images, even when they are fragmented and noisy. Our current objective is to automate a combination of the two techniques.

2. A GENERALIZED SPATIAL CORRELATION-BASED ALGORITHM FOR SELF-COHERING LARGE ANTENNA ARRAYS

Many potential applications exist for high-resolution radar such as direction finding, high-accuracy tracking, target counting, and high-resolution radar imaging. All of these applications require the use of large, thinned, random or periodic antenna arrays. Many uncertainties exist in such large antenna systems. For example, exact element positions are generally not known because of surveying problems or flexing of the large antenna structure. In addition, different channel lengths and impedance mismatches within the channels will cause electrical distortion in the array system.

Over the past 20 years self-calibration algorithms have been developed that require nothing more than data acquired from a target-of-opportunity [1]. No a priori knowledge concerning the environment is required. As this work developed, two classes of algorithms have been identified: the Dominant Scatter Class and the Spatial Correlation Class. This work shows that the entire spatial correlation class of algorithms can be characterized by one general algorithm called the Generalized Spatial Correlation Algorithm (GSCA). All of the existing correlation-based algorithms are shown to be different realizations of the GSCA.

In this paper the GSCA is derived. Then the problem of calibrating an array with this algorithm using data acquired in the near field of the array is addressed. This is extremely important since most high-resolution systems operate in the near field of the array. Finally, the relationships between the existing spatial correlation algorithms and the GSCA are presented.

Let a random source distribution $s(u)$ be illuminated by a transmitting antenna having radiation pattern $f_T(u)$. If the antenna pattern of the receiving array is $f_R(u)$ then the complex image of the source distribution is $\hat{s}_R(u) = f_R(u) * f_T(u) s(u)$ where $*$ represents convolution, and the expected image intensity is $E[|\hat{s}_R(u)|^2]$. If the data set is collected over K rangebins and the source distribution is statistically homogeneous over these rangebins then an unbiased estimate of the expected image

intensity can be formed as $g(u) = \frac{1}{K} \sum_{k=1}^K |\hat{s}_{R_k}(u)|^2$ where k is the rangebin index.

Define $p(u) = E[|f_0(u) * f_T(u) s(u)|^2] = E[|\hat{s}_0(u)|^2]$ to be the expected undistorted image intensity. Now consider maximizing the function $J = \int p(u)g(u)du$. The

maximum of this function will be reached when $g(u) = \alpha p(u)$, thus driving the array towards calibration. However, because of the Fourier relationship between an incoherent source distribution in the far field and the spatial correlation of the

received radiation in the array aperture $J = F^{-1} \text{pgl}_{\ell=0}$ where F^{-1} indicates the inverse Fourier transform and ℓ is the discrete lag index of the spatial correlation function measured in the array aperture. It can be shown that J evaluates to

$$J = \sum_{\ell=1}^{N-1} w_p(\ell) \hat{R}(\ell) \quad (1)$$

where $w_p(\ell)$ is a weighting function determined as the inverse Fourier transform of $p(u)$ and $\hat{R}(\ell)$ represents an estimate of $R(\ell)$ (the true correlation value) obtained by averaging all estimates of $R(\ell)$ available in the array. Equation (1) represents the GSCA objective function, maximization of which drives the array toward calibration. Following Hamaker et.al. [2] maximization of J enforces a stationarity constraint on the correlation values of lag ℓ measured at all available pairs of elements in the array. If $s(u)$ is a wideband, stationary process $w_p(\ell)$ depends only on the inverse Fourier transforms of the transmit and receive power patterns.

The GSCA objective function is a multiple lag objective function since the sum in (1) runs between $\ell=1$ and $\ell=N-1$. The GSCA objective function has been developed under the assumption of far-field conditions. If the data set is instead collected from the near field then the data set is spatially nonstationary and the theoretical spatial correlation function is no longer independent of the position in the array at which the correlation is calculated. Consequently there is no reason to enforce a stationarity constraint on the measured correlation values of various lags. However, depending on how far into the near field the data set originates certain low-order correlation lags will be essentially stationary across the array [3]. Therefore the GSCA can still be applied to calibrate an array using near-field data. However, potential traps do exist. The weighting function $w_p(\ell)$ is based solely on far-field assumptions and can very possibly weight heavily certain correlation lags that are nonstationary across the array because near-field conditions exist. To account for this potential problem a second weighting function must be introduced into (1):

$$J = \sum_{\ell=1}^{N-1} w_{NF}(\ell) w_p(\ell) \hat{R}(\ell) \quad (2)$$

The weighting function $w_{NF}(\ell)$ may be nothing more than a rectangular window that is zero for lags ℓ greater than the highest-order essentially stationary lag and unity for all lower-order lags. The highest-order essentially stationary lag can be determined by solving the quadratic inequality [4]

$$\ell^2 - (N)(\ell) + \frac{(0.15)\lambda R}{u_{fov}^2 d^2} \geq 0 \quad (3)$$

for ℓ , where N = the number of array elements, λ = the wavelength, R = the distance to which the array is focused, d = the interelement distance, and u_{fov} = the extent of the full field of view of the transmitter beam. The solution of the strict equality of (3) yields the largest lag that is essentially stationary across the array. It can be shown that the phase of the spatial correlation function measured in the array from radiation originating in the near field can be separated into two terms; one that depends only on the lag ℓ , and another (called the nonstationary term) that depends on both the lag and the position in the array. A correlation lag is considered to be essentially stationary across the array when the nonstationary term is less than a prescribed value. It has been found experimentally [4] that a nonstationary term less than $\pi/10$ radians has a negligible effect on the calibration process. Using $\pi/10$

radians yields the (0.15) term in (3). This term will vary depending on the upper bound chosen for the nonstationary phase term of the correlation function.

The unit-lag SCA objective function developed by Attia [5] and Subbaram's multiple-lag SCA objective function [3] are both special cases of the GSCA's general objective function (2). The objective function of the multiple-lag SCA can be obtained by setting $w_p(\mathbf{L}) = R(\mathbf{L})$ and then estimating $R(\mathbf{L})$ as $\hat{R}(\mathbf{L})$ since $R(\mathbf{L})$ is unknown [6]. The unit-lag SCA objective function is obtained in the same manner as the multiple-lag SCA but the near-field weighting function $w_{NF}(\mathbf{L})$ is zero for all lags but the unit lag.

Insight may now be gained by considering these spatial correlation-based algorithms as special cases of the GSCA. For example, from the preceding discussion on using the GSCA in the near field, it should be expected that any spatial correlation-based algorithm will breakdown when calibrating too far into the near field. However, as the calibration moves further into the near field, $w_{NF}(1)$ will be unity for fewer lags until at some point it will be unity for only the unit-lag. Moving any further into the near field will cause all lags to be nonstationary and the GSCA will fail completely. Consequently the unit-lag SCA is the most robust (in terms of near-field calibration) spatial correlation-based algorithm. Rarely is calibration done so far into the near field that the unit-lag becomes nonstationary, and hence the success Attia achieved with it.

The GSCA can be used to gain even more dramatic insight into Tsao's Energy Conservation Algorithm (ECA) [7] which has previously been thought to represent another class of self-calibration algorithms. The algorithm is based on Parseval's Theorem and the objective function used by Tsao minimizes the difference between the total energy in the array aperture and the total energy in the image within a specific angular sector determined by the field of view of the transmitter beam. Since the total energy within the aperture is constant, minimizing Tsao's objective function is equivalent to maximizing the total energy within the specific angular sector in the image. Therefore an equivalent ECA objective function is [1]

$$J_1 = \frac{1}{K} \sum_{k=1}^K \int_{-\Delta u/2}^{\Delta u/2} |\hat{S}_k(u)|^2 du \quad (4)$$

However, this objective function is nothing more than J with $p(u) = \text{rect}(\Delta u)$. Therefore the ECA is another spatial correlation-based algorithm with $w_p(\mathbf{L})$ equal to a sinc function.

Figures 1 and 2 demonstrate the effect of the weighting function $w_p(\mathbf{L})$ in (1). The array was calibrated on a simulated source distribution which contained 10 rangebins each with 2 point sources randomly distributed over an angular extent of 0.167 radians except the first rangebin which had one source located at zero radians. Figure 1 shows the image of the first rangebin obtained after calibrating the array with the GSCA using the appropriate weighting function $w_p(\mathbf{L})$ determined by $p(u)$. This diffraction limited image clearly demonstrates the array has been calibrated correctly. Figure 2 shows the image of the same point source obtained by calibrating with the GSCA using an incorrect weighting function corresponding to a rectangular function in the u domain of much less angular extent

than is illuminated by the transmitter. The effect of using the incorrect weighting function is seen by the distorted image of the point source in Figure 2. The ECA was developed by Tsao as an independent algorithm. Now with the understanding that the ECA is really a correlation algorithm it can be seen that the ECA will only work well in simulations. This is because the rectangular function $p(u)$ implies that no energy was radiated or received outside of the mainlobe of the system. This is not true in practical systems where energy is always radiated and received outside of the mainlobe by sidelobes. Consequently, $w_p(L)$ equal to a sinc function describes an unrealizable situation.

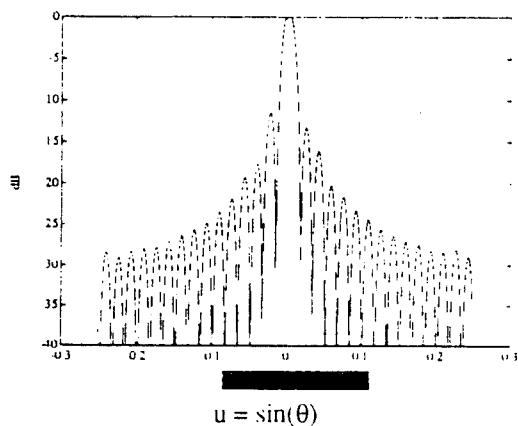


Figure 1. Image of a point source located at $u=0$ with $p(u) = \text{rect}(0.167 \text{ radians})$.

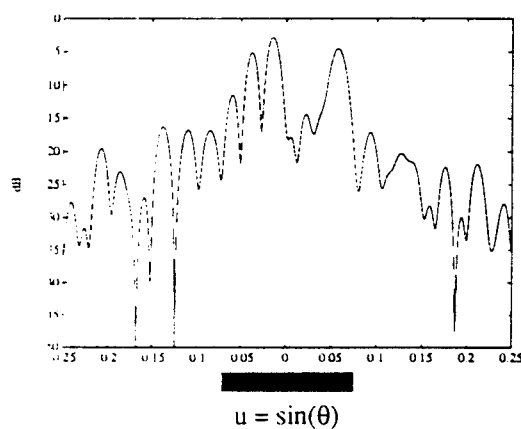


Figure 2. Image of a point source located at $u=0$ with $p(u) = \text{rect}(0.01724 \text{ radians})$.

The GSCA is an important generalization of the existing spatial correlation-based algorithms. The generalized objective function provides a basis from which analysis applicable to the entire spatial correlation class can be carried out. One such important analysis is the derivation of a tolerance theory for this class of algorithms similar to the theory that already exists for the Dominant Scatterer class [8].

3. 2-D HIGH RESOLUTION MICROWAVE IMAGING OF GROUND VEHICLES WITH A UWB RADAR SYSTEM

INTRODUCTION

During 1989 a system was developed at VFRC for the detection of inert military landmines.⁹ Since such mines are very limited in size, it was important to develop resolution cells that were as small as possible. An S-band radar set with 1 GHz bandwidth was developed for this purpose. This UWB radar system provided a range resolution of 15 cm in air. It was only a short time after the completion of the mine detection program when this equipment was applied to the imaging of larger, ground based surface targets.

This paper will explain both the design of this system and the extensions which were made during 1991 to allow operation in three diverse frequency bands. A variety of target images from the resulting experiment program will also be presented.

IMPORTANT FEATURES OF THIS PROGRAM

The original imaging system developed in the mine detection effort used a 1 GHz bandwidth with a center frequency of 3.5 GHz. The fractional bandwidth (0.286) therefore classifies this system as a stand-alone, ultra-wideband radar.¹⁰

It was very clear, however, that the wideband video and digital components operated independently of the center microwave frequency. Equipment from a variety of past programs was available which allowed additional front ends to be constructed at center frequencies of 9.6 and 16.8 GHz. Thus the same targets could be imaged at three different frequencies representing a total span of more than two octaves. Although 1 GHz bandwidth systems at the higher two frequencies are not classified inherently as UWB radars, their combination forms a system of enormous bandwidth (although measured at discrete intervals). This represents a concept of spectrum conservation which may prove important in the future growth of UWB system concepts.

A further important result of this work was the production of images with two-dimensions as contrasted with the traditional range/amplitude profiles. As will be shown later, one-dimensional range scans are useful and provide important input to target identification and classification algorithms. The two-dimensional image, however, adds angular resolution to provide another important source of information.

SYSTEM DESIGN

The simplified block diagram of the three-band UWB radar system is presented in figure 3. This design insured that the video and digital sections were frequency independent in order to minimize the cost of system development. Only one modular radar system was constructed. The array was formed by physically moving the front end to each specified sampling position. Each of the three systems was fully coherent, and the experiments were virtually time insensitive. This design also permitted great flexibility in reconfiguring the equipment for a variety of experiments. The only disadvantage of the synthetically formed array was that only stationary targets could be imaged. This did not prove to be a liability, however, since a large variety of suitable objects was available.

Although three frequencies were in use, the block diagram for each band was the same. A single microwave oscillator was used to provide both the transmitted pulse and the coherent reference for the phase detector. The 1 nsec pulse (3 dB) was formed by a New England Microwave series 6500 pin diode switch. The peak power level from this device was on the order of 1 mW. A free-running HP 8082 pulse

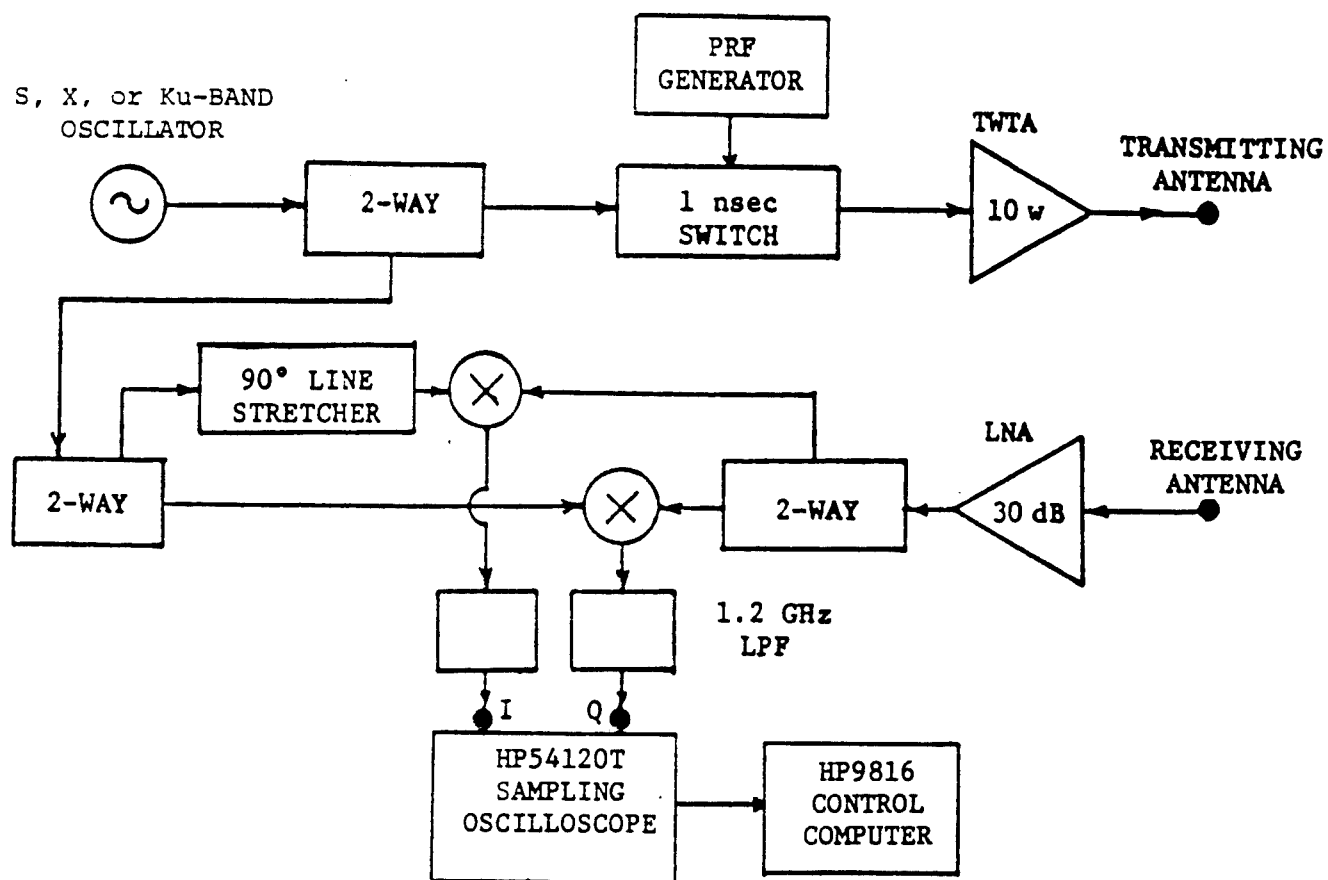


Figure 3. Block Diagram of the Three Frequency UWB Radar System.

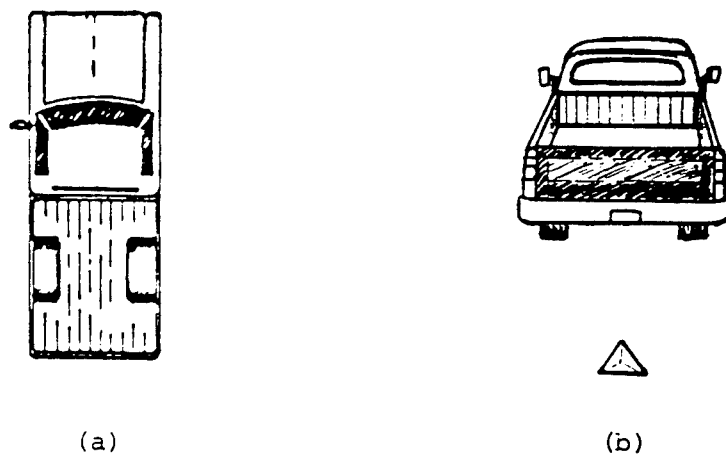


Figure 4. Pickup Truck Target (length, 5.4m, width 2m, length of bed 2.5m).
 (a) Overhead plan view
 (b) In perspective as viewed from the array

generator was used to provide the gate to the switch. It also established the PRF of the system at a rate of approximately 100 kHz.

Amplification of the power level was accomplished by external solid state or TWT amplifiers. Maximum power output was limited to 10 Watts.

Separate horn antennas were used for the transmitter and receiver in each system. The use of a T/R switch was not considered due to the very close range of the targets. The gains of the horns for the three band system varied from 18 to 24 dB. Due to the extreme near field conditions of the experiments, the antennas were continually repointed at the target complex as they were moved to each successive sampling location. The noise figure of the system was established by a low noise amplifier connected to the output of the receive horn.

The phase detector is based on a pair of dc-coupled, wideband mixers. Two circuits were built. One for S-band alone and the other for both X and Ku-bands. The 90 degree line stretcher was adjusted each time the system was changed between the two higher frequencies. Since the inputs to the phase comparator were of identical frequency, the baseband output was a dc level proportional to the amplitude and phase of the input signals. This level persisted for the length of the radar echo. (1 nsec) Thus the filtered output of the phase comparator contained the quadrature signals required by the image processing software.

The transmitter is obviously a key component in the development of a UWB radar system, but an effort of similar magnitude exists in providing an A/D converter capable of digitizing waveforms with very wide bandwidths. The HP 54120T is a sampling oscilloscope that is operational from dc to 20 GHz. Thus not only can the actual transmitted RF waveform be displayed, but the baseband I and Q signals can be digitized and stored in RAM for downloading to the control computer. The sampling interval can be set as low as 10 psec, thus removing the speed of the digitizer as a limiting factor in an experimental program. Waveforms can also be averaged to improve the SNR. The only disadvantage of the instrument is the time required to complete the sampling procedure (approximately 10 seconds for x32 averaging). Since the targets are stationary, however, this restriction is not significant. The oscilloscope is connected to an HP9816 desktop computer through the HP-IB interface line. This allows convenient transfer of data sets to floppy discs for permanent storage.

As a summary of the operating features of the system the parameters of the S-band set are summarized below:

center frequency	3.5 GHz
wavelength	0.0857 meters
pulse width (3 dB)	1 nsec
system bandwidth (3 dB)	1 GHz
peak transmitted power	0.1 W to 10 W as needed
noise figure	3 dB
antenna gain	18 dB
antenna beamwidth	20 degrees
minimum range	no limit
maximum range	approximately 250 meters
array type	monostatic synthetic aperture

EXPERIMENT PROGRAM

The overall objective of this phase of the program was to study the images of complex targets under ideal conditions. In previous experiment programs the targets under study were often placed in complex surroundings at long range. In order to maximize the image quality the current tests were conducted at close range on a clear section of field. After these studies have been completed, it will be

very important to repeat them in more typical environments with both foliage and ground clutter. The targets were positioned approximately 10 to 15 meters from the array, and the angular resolution required to match the 15 cm range cell was on the order of 10 mrad. Each array was 50 wavelengths long, and element sampling was conducted each half wavelength. Thus the array lengths were: 4.24 m at S-band, 1.55 m at X-band, and 0.88 m at Ku-band.

Since the system had already been constrained to image only stationary targets, the synthetic aperture technique was used to measure sufficient element positions to form a filled, periodic array. Future experiments with array thinning may show the usefulness of this time saving procedure.

Both transmitter and receiver were moved to each successive sampling position as the synthetic aperture was formed. The resulting monostatic array, when coupled with 15 cm range resolution, provided the potential for very detailed images.

RANGE/AMPLITUDE EXPERIMENTAL RESULTS

Range/amplitude presentations have traditionally been used to describe radar cross section profiles at a specified aspect angle. This is a very useful method for gaining insight into certain characteristics of the targets under study. It has the added advantage that no signal processing is required, thus allowing the results to be observed immediately. In fact, research at VFRC on using neural networks to classify targets from range/amplitude profiles has shown promise of successful operation.

A typical target used in this program was a conventional, full size pick-up truck. The following discussion will focus on this object in order to provide a detailed analysis of the resulting images. The truck was initially positioned in a clear section of field on the VFRC test range facing away from the array as shown in figure 4.

The radar equipment viewed the target area from a platform approximately 12 degrees higher in elevation. S-band was the first frequency chosen for the tests. The equipment was configured for vertical polarization and positioned at the array center. The range profile shown in figure 5 was observed. Notice that six distinct scattering centers are observed in the region between 6 and 20 meters in range. The first, located at approximately 7 meters, is a small (1 foot in dimension) corner reflector used as a reference target. Large specular reflections from both the tailgate and the rear of the cab are found at 9 and 12 meters, respectively. The responses between 14 and 20 meters, however, did not correspond to any targets in position on the field. It was soon determined that they were from multiple reflections between the tailgate and the cab in the bed of the truck.

In order to verify that this was the correct interpretation of these echoes, the tailgate was lowered without moving either the truck or the radar set. This eliminated the multiple reflections as shown in figure 6. The response of the rear of the cab was much larger in this case since the scattering surface of the tailgate had been significantly decreased.

After replacing the tailgate in its original closed position, the first synthetic aperture experiment was conducted. During this procedure, the radar set was moved over a distance of 4.24 meters. This corresponds to a variation in aspect angle of approximately 25 degrees at the rear of the truck. The multiple reflections were observed (with varying amplitude) over this entire angular extent. Variation in elevation was tested between 7 and 30 degrees. Again, the multiple reflections were identified in each experiment. Their amplitudes peaked, however, between 10 and 15 degrees.

Experiments were also conducted with horizontal polarization. The character of the truck response was very similar to that observed with vertical polarization. The multiple reflections, however, were significantly decreased in level.

Amplitude
Max = 1308

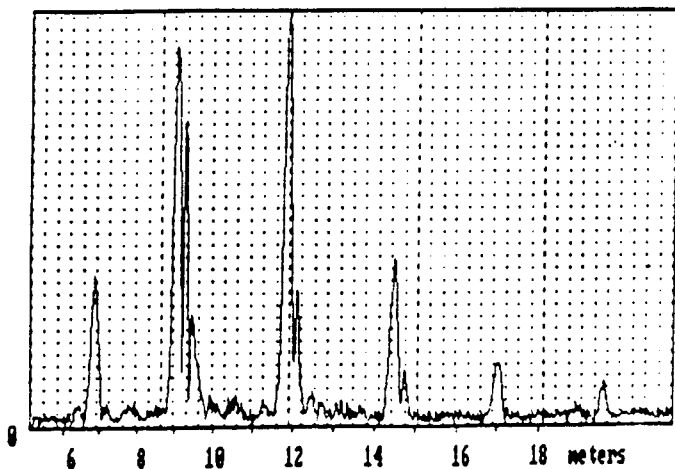


Figure 5. S-band Pickup Truck.
Rear view at array center
showing multiple reflections.

Amplitude
Max = 4361

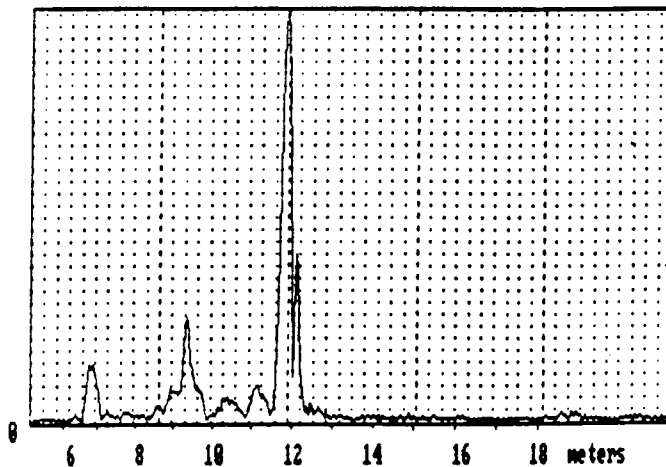


Figure 6. S-band rear view with
tailgate lowered showing
only cab and tailgate
reflections.

Amplitude
Max = 4816

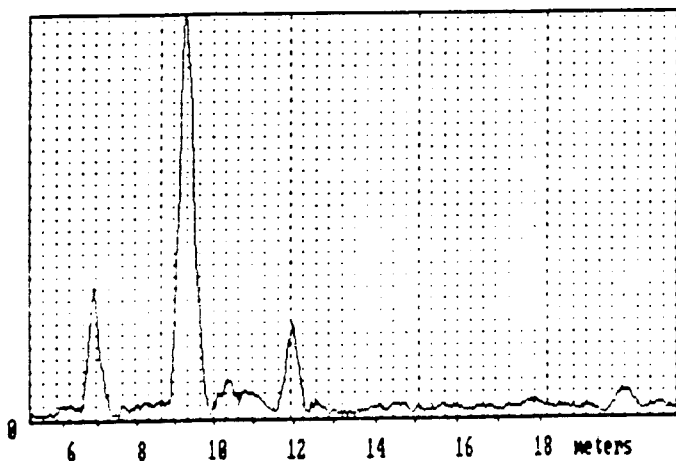


Figure 7. X-band rear view.

Amplitude
Max = 495

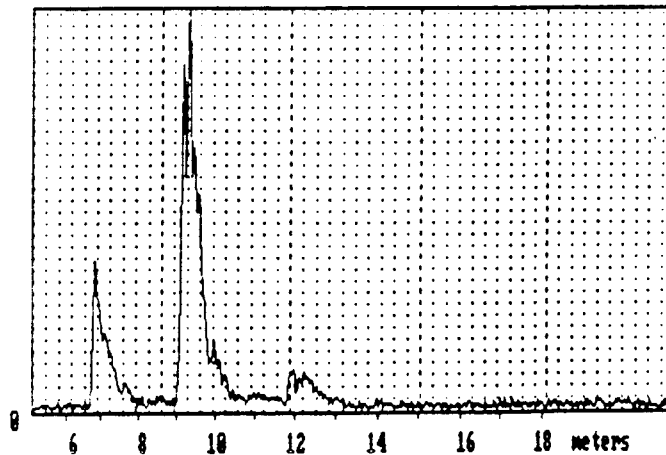


Figure 8. Ku-band rear view.

The results from tests conducted at X and Ku-bands are also of interest. They both showed very large specular reflections from the tailgate and reduced responses from the cab. At these higher frequencies, the multiple reflections were so small as to be almost unidentifiable. These range/amplitude profiles are shown in figures 7 and 8. They again represent the rear view of the truck from the array center.

For a more complete understanding of the scattering properties of the truck it was examined at a variety of aspect angles. Shown here are the results of S-band tests where the truck was viewed from the rear but 38 degrees off axis (figure 9), parallel to the array (figure 10), and from the front (figure 11). In each of these cases at least one multiple reflection was clearly identified. It should be noted, however, that large differences in both amplitude and multiple reflection delay are very apparent and tend to verify that the one-dimensional radar signature of the vehicle is quite dependent on aspect angle. Despite their complexity, these high resolution amplitude/range plots are nevertheless very informative in attempting to classify this object as a small truck.

TWO-DIMENSIONAL IMAGING PROGRAM

Further ability to identify the target may be obtained by adding a second dimension to the range/amplitude display. After the quadrature target echoes have been measured at each of the sampling positions in the synthetic aperture array, several procedures are used to produce a two-dimensional image. First, the echoes must be aligned to compensate for the variation in range as the radar set is moved along the array. This is strictly accomplished according to the geometry of the experiment. Since the range cell is only 15 cm in depth, however, this procedure must be conducted not only for each range bin but also for individual scan angles. It is, therefore, a time consuming step in the image processing.

The phased array itself is produced offline using adaptive beamforming to compensate for errors in the position of the radar module during the experiment. This is a blind-equalization means of self-calibrating a distorted antenna array. The target echoes received by the antenna elements have been randomly modulated in phase by the element position errors. The adaptive beamforming processor extracts information from the measured phase of the reference reflector from which it calculates the required correction for each element's measured phase values. Figure 12 shows the point source response of the X-band array. Note that the abscissa in this plot is cross range, not range as in the previous examples. This is one range slice of the 80 which are used in forming a two-dimensional image. It covers the range of the small reference corner reflector, and demonstrates the 10 mrad angular resolution of the array. Attempts to process this data set without using adaptive beamforming resulted in a distorted output image. This verified that the tolerance on element location was not adequate during the experiment to allow for the use of conventional array processing techniques.

The two-dimensional images for the pick-up truck viewed from the rear are shown in figures 13 (S-band), 14 (X-band), and 15 (Ku-band). As was noted in the range/amplitude profiles, the multiple reflections are prominent in the S-band experiment but very small at the higher frequencies. The reflection from the rear of the cab is similarly dependent on the band. As the frequency rises, its amplitude decreases. The image, in fact, becomes more specular and less recognizable optically as the frequency is increased. The angular dimension in these plots, however, makes visual identification of the target as a small truck possible.

Another advantage of the two-dimensional presentations is that diversity techniques may be used to further improve the image. Shown in figure 16 is a demonstration of combining the three maps shown previously (figures 13, 14, and 15) to form a composite image representing the characteristics of all three frequencies. The multiple reflections, large speculars, and target detail of each individual frequency range are apparent in this image. In effect, this plot represents a UWB radar system with discretely sampled bandwidth of over 14 GHz.

Amplitude
Max = 2219

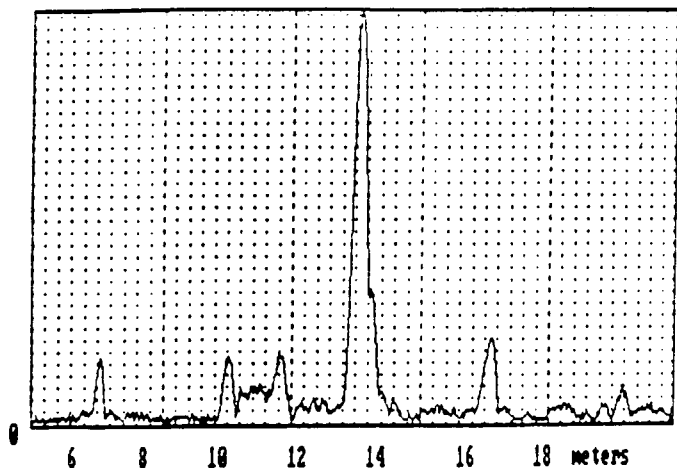


Figure . S-band view from rear,
38 degrees off axis.
(Pickup truck)

Amplitude
Max = 1682

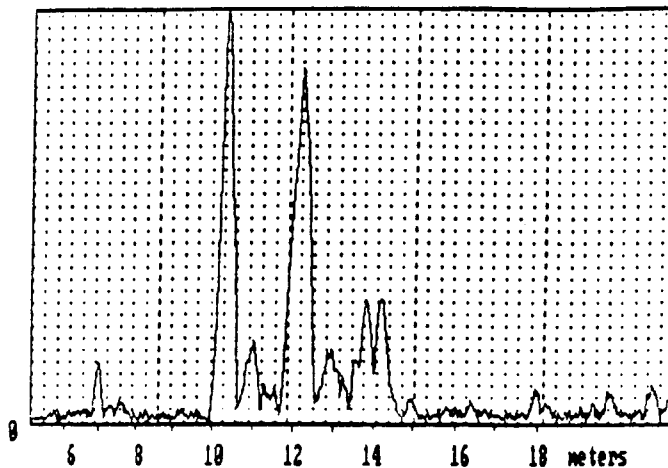


Figure 10. S-band broadside view.

Amplitude
Max = 1351

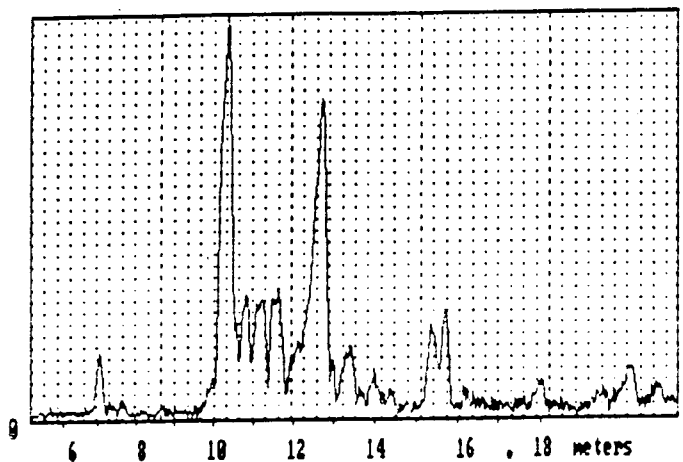


Figure 11. S-band front view.

AMPLITUDE
MAX = 1228

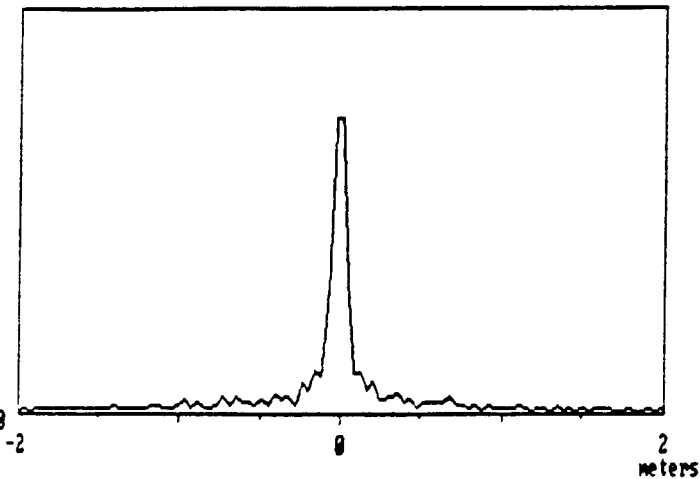


Figure 12. X-band specular reflector
image illustrating angular
resolution of array (10 mrad).

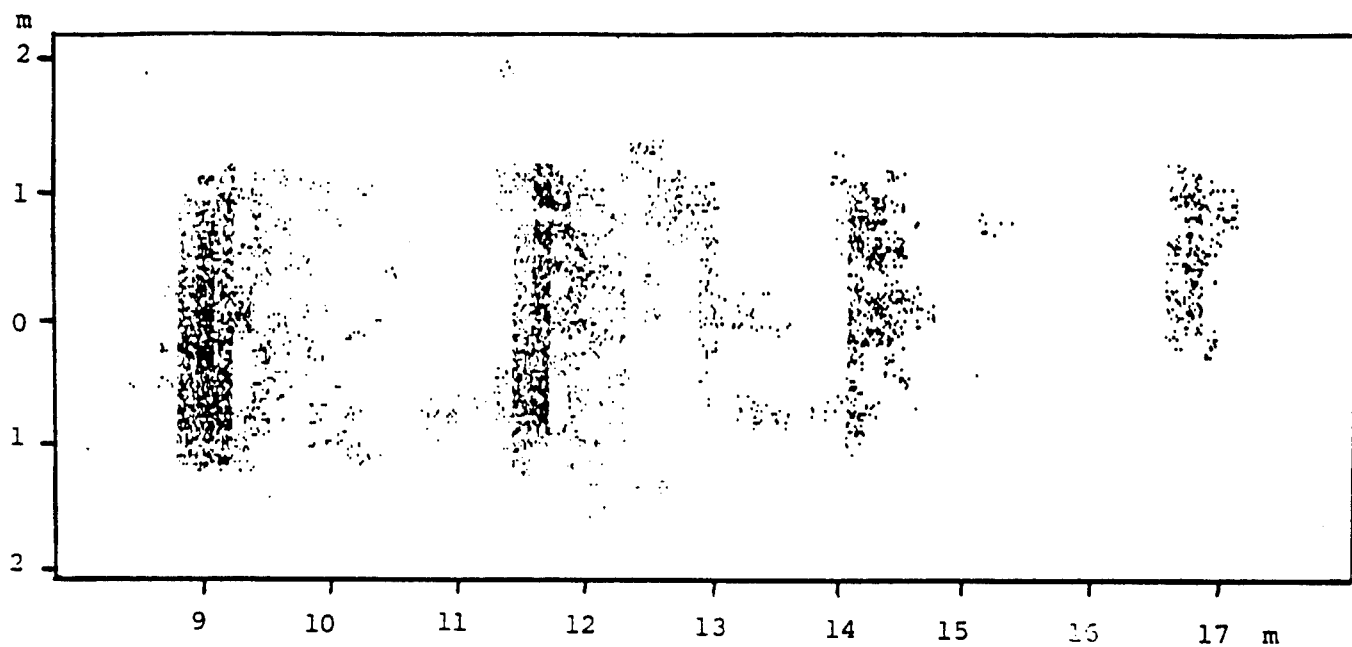


Figure 13. S-band rear view image in two dimensions. (Pickup truck)

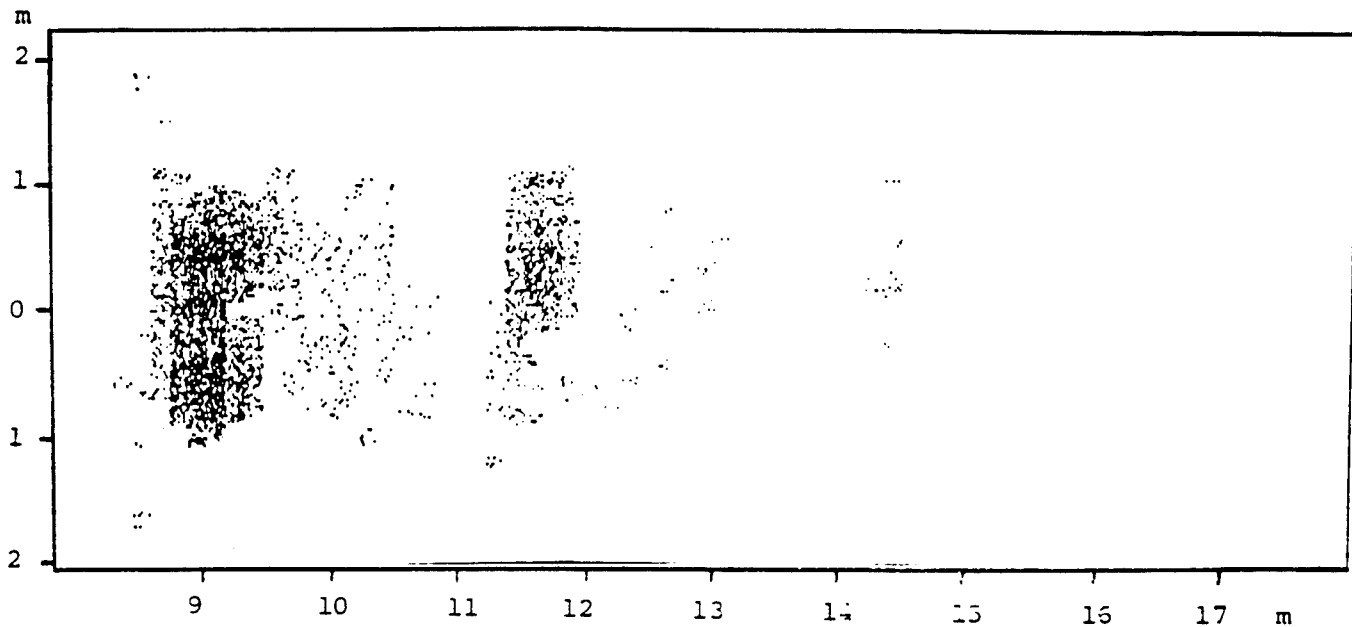


Figure 14. X-band rear view image in two dimensions.

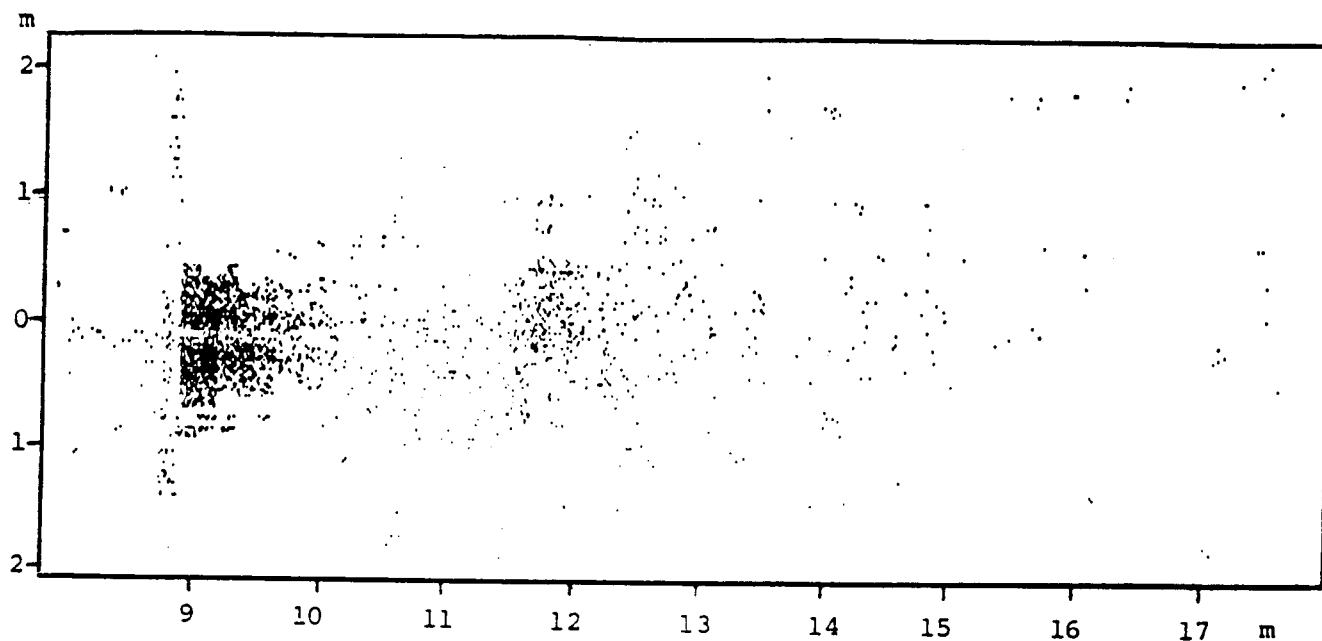


Figure 15. Ku-band rear view image in two dimensions. (Pickup truck)

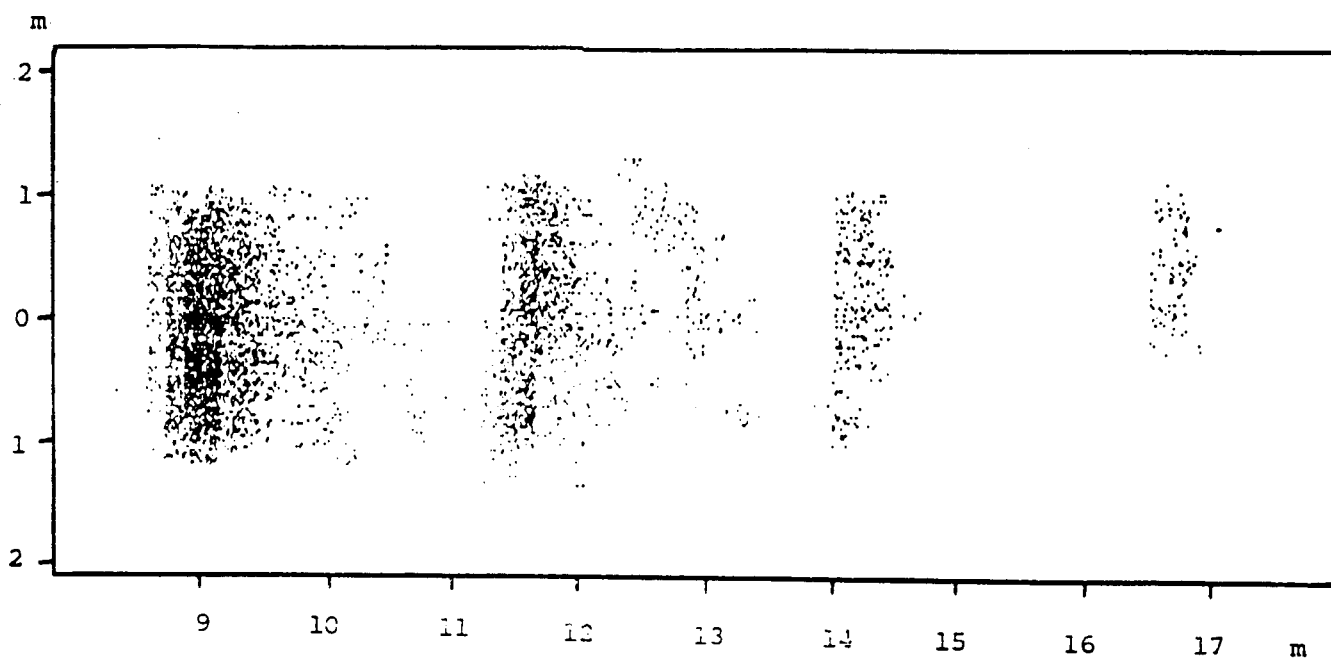


Figure 16. Rear view of truck, composite image created by summing figures 11, 12, and 13. The image contains the important features of all three frequencies.

4. ENHANCED TARGET DETECTION USING STEREOSCOPIC DISPLAY TECHNIQUES

INTRODUCTION

In an experiment performed at the Valley Forge Research Center, it was observed that target detection sensitivity could be increased by using high resolution microwave imaging in two and three dimensions [11]. Continued research during this period comprised three tasks. The first was a critical analysis of the experimental procedure and an interpretation of the results. Secondly, a study was made of three-dimensional perception and display in order to gain better understanding of the mechanisms involved. Finally, applications were considered to determine where this technology may prove most useful.

EXPERIMENTAL ANALYSIS

In the first part of the experiment, detection sensitivity was plotted against target-to-clutter ratios (TCR) for 0-dimensional and 2-dimensional targets. The definition of TCR used in the experiments is given as

$$\text{TCR} = \frac{\text{Average Power per Pixel in the Target}}{\text{Average Power per Pixel in the Clutter}}$$

The reported result was that the 2-D targets could be detected with equal probability at TCR's 11dB lower than the 0-D targets. In the second part of the experiment, detection sensitivity was compared for 3-D and 2-D targets. This resulted in equal detection at TCR's an additional 7dB lower.

Correction

During this period, a minor error that bears mentioning was discovered in the first part of the experiment. In the 0-D case, the target pixel replaced a clutter pixel in the final image. However, it should have been added coherently to the clutter as in both the 2-D and 3-D cases. As a result, the target power used to determine the TCR in the 0-D case was larger than it should have been. We can determine approximately what the target power was by subtracting from this value the average clutter power. The correction for the TCR was performed and the new 0-D curve is displayed in Figure 17. For high TCR's the correction is negligible and, therefore, the result

reported earlier still stands. That is, for high TCR, it does not matter significantly whether the target replaces or is added to the clutter.

Conclusions`

In the earlier report, the improvement in detection sensitivity was attributed to the increased target dimensionality. During this period, we determined that the improvements that were witnessed were the result of two factors.

In the first part of the experiment, the improvement is not merely a result of increased dimensionality, but of the increased resolution at which the target is displayed. This is easily seen when the 0-D target is merely considered to be a very small 2-D target. Now both targets have the same dimensionality, but the target with the finer resolution, the 2-D target, has a much lower threshold of detection. When the resolution of the target is increased, the target occupies more pixels in the image. Since each pixel conveys additional information, it becomes easier to detect the target as the resolution becomes finer.

The 0-D case can then be interpreted as the limiting case for 2-D as the resolution cell grows larger than the size of the target. Therefore, we can expect that the 2-D curve in Figure 17 will approach the 0-D curve as the resolution cell grows. Similarly, it may be possible to shift the 2-D curve even farther away from the 0-D curve by improving the resolution of our imaging system.

In the second part of the experiment, the improvement is a result of the observable depth difference between the target and the clutter in the three-dimensional image [12]. The manner in which this depth difference is achieved is discussed in the next section. For now, however, we can state that the 2-D case is the limiting case of 3-D where the depth difference is decreasing. Therefore, it is important to determine the factors necessary to produce these large differences.

THREE-DIMENSIONAL PERCEPTION AND DISPLAY

Because of the obvious benefit of three-dimensional detection, a study was undertaken to gain a better understanding of the mechanisms involved in the display and perception of three-dimensional images. What follows is a brief introduction to some key points.

Disparity

When we look with two eyes at an object, each eye sees a slightly different image of the object since the viewing positions of the left and right eye are different. This phenomenon is known as stereo vision or stereopsis and can be experienced, for example, by looking at your index finger while alternately opening and closing each eye. What you will see is that the horizontal position of your finger will appear to shift with respect to the background. The brain

uses this shift to judge the distance between your finger and the background. The mechanism of judging distance based on the perceived differences in the images provided by each eye is known as binocular parallax or binocular disparity and is further demonstrated using Figure 18,

When the two eyes focus on a point, denoted by A in this figure, the eyes rotate until the focused point is projected onto the centers of the retinae, labeled A'. All other points, such as point B, "fall where they may" in the retinal image. Notice that the separation of A' and B' is larger in the right retinal image than in the left. These separations are typically measured as angles and are denoted by Θ_1 and Θ_2 in the figure. The disparity of a point is defined as the difference of these angles and is given notationally as

$$\eta = \Theta_1 - \Theta_2$$

It can be shown that the perceived distance between the points A and B is directly proportional to the disparity of point B. It follows that, for our purposes, larger disparities will normally result in better separation between the target and background clutter.

The disparities that the brain can detect vary from person to person and have also been found to be dependent on the size of the stimulus used. Current literature suggests that, for the large targets used in our experiment, depth differences should typically be perceived for disparities ranging from about 10" to 2° [13]. For disparities above this range, the brain experiences difficulty fusing the images to form a three-dimensional scene. In fact, even within this range, fusion may often take a considerable amount of time for large disparities. The perceivable range of disparity is an important factor to consider in the production of the three-dimensional images displayed in our experiments.

In Figure 19, we demonstrate how the 3-dimensional scene of Figure 18 can be reproduced by showing the eyes two separate 2-dimensional views of the scene. Notice that the separations of A' and B' are identical to those experienced in Figure 18. The result is that the brain is "tricked" into believing that the eyes are viewing a 3-dimensional scene. As before, the disparity is the difference between the angular separations Θ_1 and Θ_2 . For the typical case, where Θ_1 and Θ_2 are small,

$$\Delta_1 \approx D \sin \Theta_1 \approx D \Theta_1$$

$$\Delta_2 \approx D \sin \Theta_2 \approx D \Theta_2$$

and

$$\eta = \Theta_1 - \Theta_2 = \frac{\Delta_1 - \Delta_2}{D} \quad (\text{radians}) \quad (5)$$

From equation (5), then, it is clear that the disparity of a point is directly proportional to the difference in its horizontal position in the two images. Therefore, as long as the disparity does not exceed the detectable range, large horizontal shifts of the target should be easier to detect than smaller shifts.

Stereoscopes

When the eyes observe two dissimilar scenes as in Figure 19, muscular movements must be made to correctly align the images on the retinae. If the scenes are large and cannot be placed very close to one another, these movements are very difficult, and correct alignment of the images may be impossible to obtain. The introduction of the first stereoscope in 1838 by Sir Charles Wheatstone alleviated this problem. Many stereoscopes have been developed since then, all having the same purpose. The stereoscope used at the Valley Forge Research Center is based on a design proposed by Sir David Brewster in 1849 and later improved by Oliver Wendell Holmes. It is comprised of a pair of lenses and its function is demonstrated in Figure 4.

In Figure 20, the normal vision of a single photograph is shown. Remember that when both eyes see the same image, as they do here, there are no disparities and, as a result, no depth is perceived. In Figure 21, we demonstrate the use of the stereoscope to view a stereo pair. The image of each photograph, denoted by the solid lines, is refracted at the lenses before entering the eyes. Notice that the positioning of the eyes and the retinal placement of the images are exactly the same as in Figure 20. As a result, the observer believes he is looking at a single photograph outlined by the dashed lines. Now, however, since the images originate from dissimilar photographs, disparities are present and the observer perceives the photograph in depth.

In working with the stereoscope, it has been observed that the separation of the target and clutter may sometimes be more easily detected by looking into the lenses at an angle, rather than head on. Another observation is that it takes some people considerable amounts of time in their first attempts to fuse the images. But after their eyes have "learned" to correctly align the images, their ability improves. These findings suggest that an individual's ability to successfully detect targets in clutter may improve with training.

POTENTIAL APPLICATIONS OF 3-D RADAR IMAGING

Detection Of Moving Targets

The experiments discussed emulate this scenario. A single radio camera is mounted on a satellite or high flying aircraft and aimed towards the ground. Successive pictures are taken and observed stereoscopically. The radar returns from the ground will be identical in the two images and therefore will not be observed in depth. However if a target has moved during the time in

which the pictures are taken, it will appear in different locations in the two images and will be observed separate from the clutter.

When the movement of the target can be displayed as a purely horizontal shift, as in the experiment, the size of the shift is proportional to the speed of the target. Since the perceived distance between the target and clutter is proportional to this shift, the speed of the target can be estimated from the separation of the target and clutter in the 3-D image. In this manner, targets with small radar cross-sections can be differentiated by the speeds at which they are moving.

Detection of Static Targets

Two radio cameras focused on the same location simulate eyes operating at microwave rather than optical frequencies. In applications such as locating targets below the surfaces of land and water, the target can be located in both position and depth. In another scenario, two cameras mounted to satellites could determine the locations of flying aircraft since the aircraft targets would be observed above the earth background..

CONCLUSIONS

It is clear that there is great potential for three-dimensional radar systems in the area of detection. By increasing the dimensionality of the detection system, it has become possible to identify targets that would not be detected otherwise. During this period, we have isolated the factors necessary to obtain this high level of detection, namely high-resolution and large disparity.

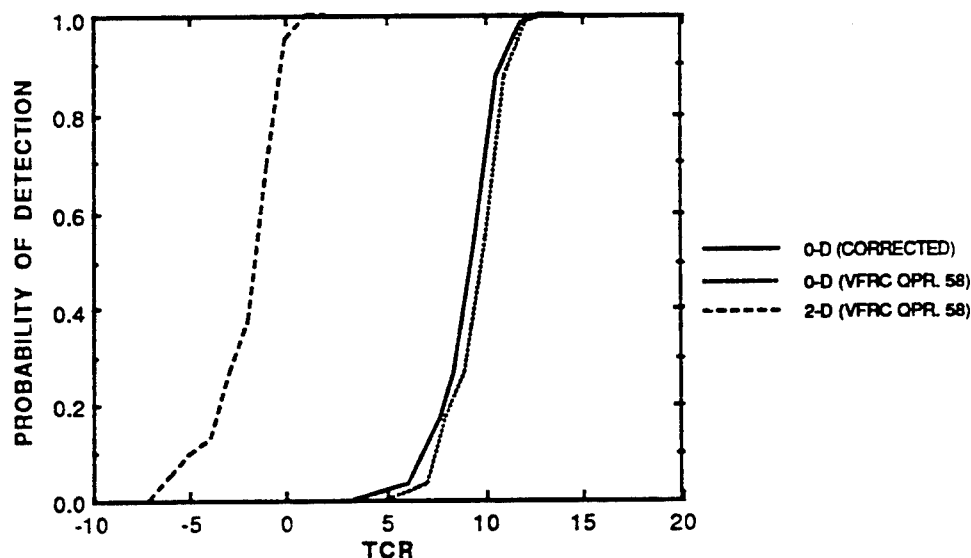


Figure 17. 2-D detection versus 0-D as a function of TCR.

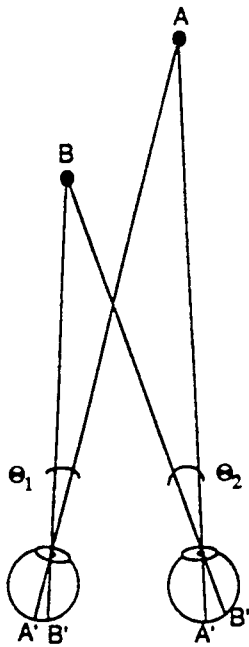


Figure 18 Stereo Vision of a Three-Dimensional Scene.

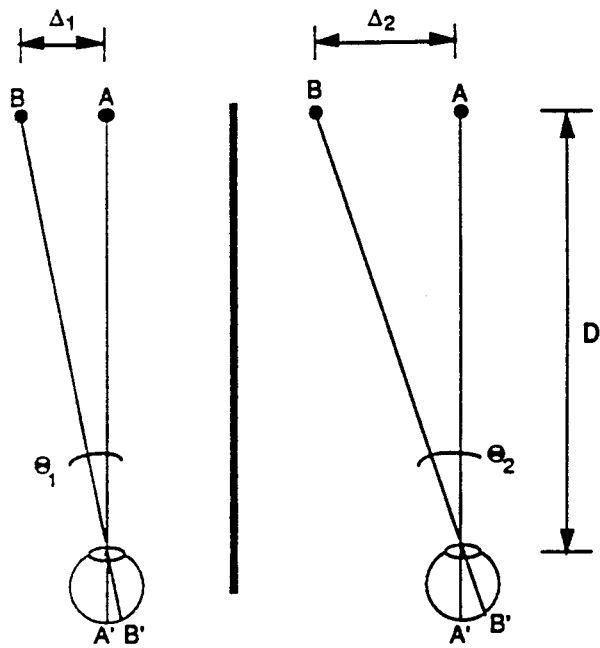


Figure 19 Reproduction of a Three-Dimensional Scene.

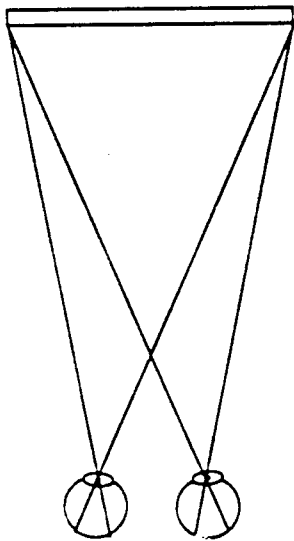


Figure 20 Normal Vision of a Photograph.

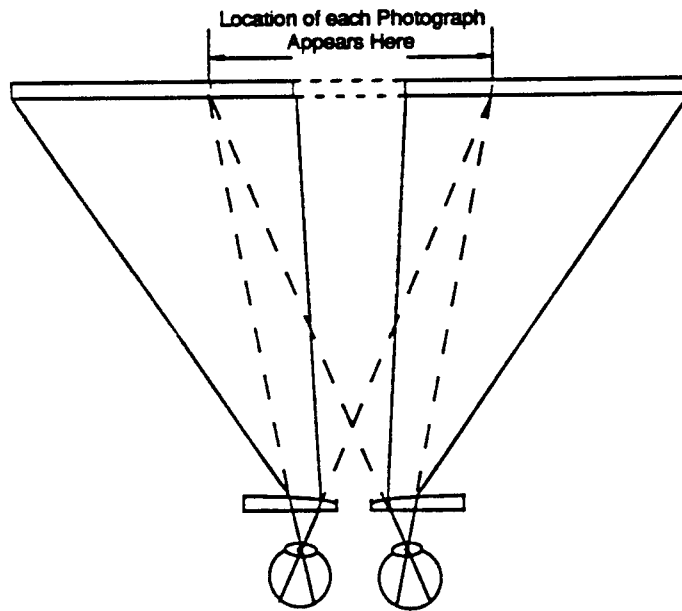


Figure 21 Vision of a Stereo Pair With Lenses.

5. AUTOMATIC TARGET RECOGNITION USING NEURAL NETWORKS FOR MICROWAVE IMAGING SYSTEMS: PRELIMINARY REPORT

OBJECTIVE

Two-dimensional, high resolution microwave imagery has proven to be a powerful tool in the recognition of radar targets [1]. The objective of the proposed effort is to extend this recognitive capability to automatic target recognition by using artificial neural networks. The neural networks developed will be able to correctly recognize and classify fragmented (incomplete), distorted, or noise-corrupted imagery obtained with microwave imaging systems.

INTRODUCTION

Microwave imaging systems, which combine radar with adaptive signal processing techniques, have achieved two-dimensional high resolution images of aircraft. The processing is based on advanced signal-imaging algorithms [1]. Several radio camera systems currently in operation at the Valley Forge Research Center of the Moore School demonstrate the capability of microwave imaging systems to produce images suitable for target recognition. Fig. 22 illustrates a high quality two-dimensional image of an L-1011 approaching the Philadelphia International Airport. A plan-view drawing of the airplane is shown in Fig. 22 to facilitate comparison.

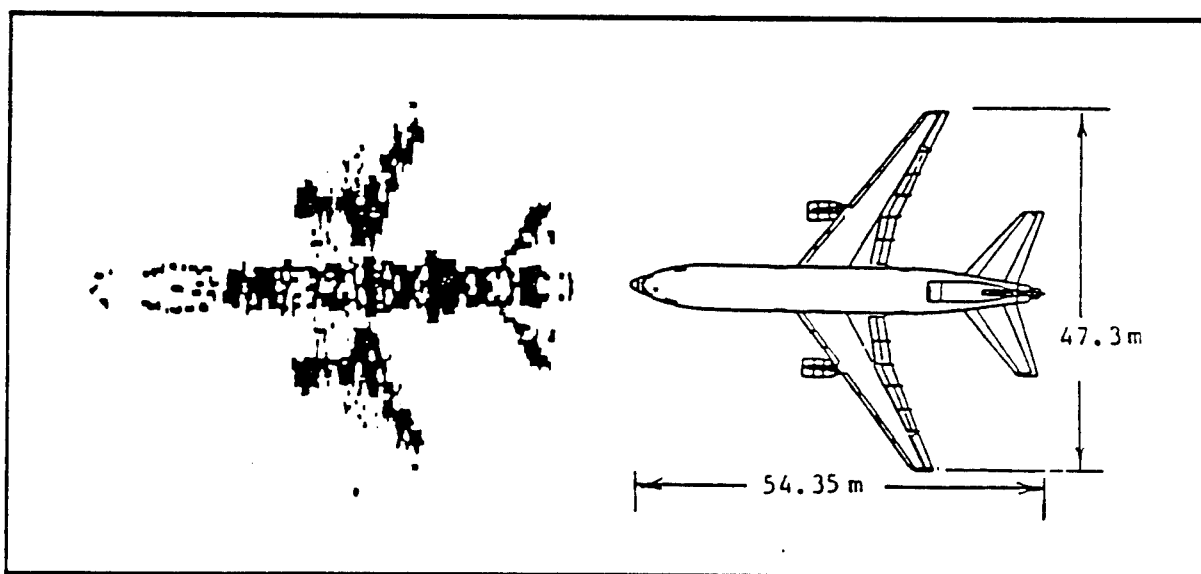


Figure 22 Microwave image of L-1011 obtained with microwave imaging system: (A) Microwave image. (B) Plan-view. The radio camera operated at X-band (3 cm wavelength) with 150 MHz bandwidth. The aircraft distance was approximately 2.5 KM.

The high quality exemplified by the microwave image of Fig. 22 however, is sometimes

lacking because of factors such as random glint, scintillation, background clutter, inadequate dynamic range, system noise, and compensation error. The images may be fragmented, distorted, or severely corrupted by noise, to the extent that a human observer is unable to recognize the target. Two examples are shown in Fig. 23.

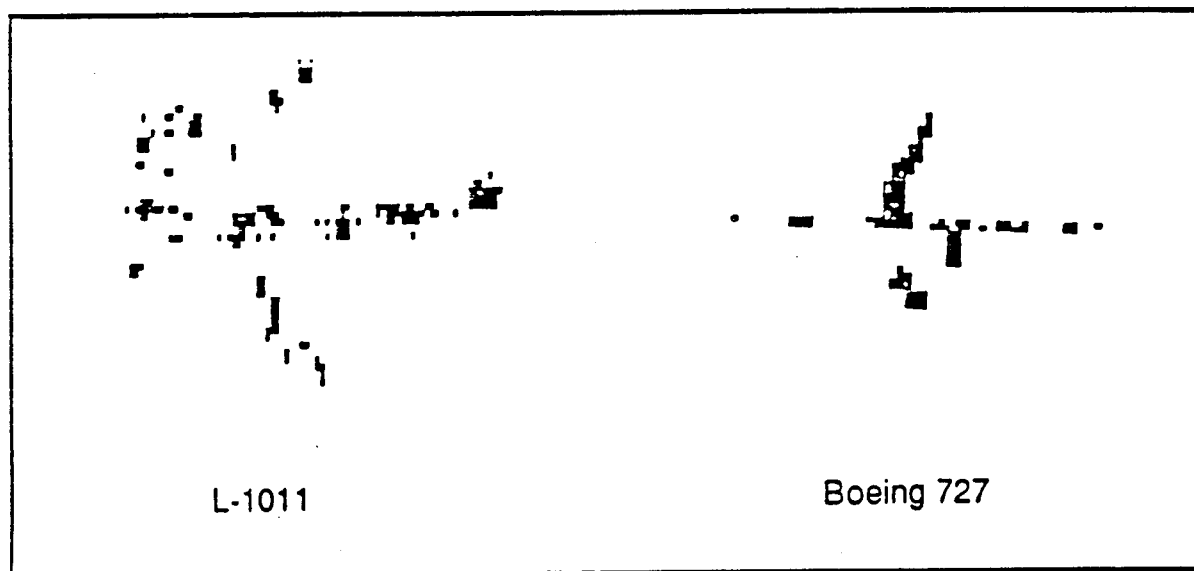


Figure 23. Two examples of fragmented microwave images : an L- 1011 and a BOEING 727.

In order to improve the 2-D images, diversity combining techniques may be introduced in the imaging procedure. Several incomplete "raw" images derived from different angles, frequencies, or polarizations can form a superior image by overlapping or averaging. Fig. 24 shows the diversity process exercised on several images of a Boeing 727. The upper row shows five, independent "raw" images, each highly fragmented. The lower row shows that 2nd and 5th order diversity lead to less fragmented images. Unfortunately, this technique is not practical for those applications in which the time required for data acquisition and processing is too long. This problem becomes even more significant when multiple frequencies and polarizations are introduced. Thus the ability of neural nets to recognize highly fragmented targets is very important.

In theory, obtaining a perfect 2-D image of a target requires an infinite antenna array to collect all the information over the entire range of frequency and polarization. Using an infinite array means that a δ -function radiation pattern scans across the target. Measuring over the entire frequency range means that the target is illuminated by an impulse of infinitesimal extent to obtain extremely high range resolution. Measuring with all polarizations produces still more information about the target. In practical applications, however, the amount of information that can be gathered is always limited. A 2-D image is formed only from partially available information in a noisy environment.

In addition, the 2-D images obtained with microwave imaging systems are only projections in range and angle of the original 3-D objects. Different projections will be produced at different elevations. In other words, the image of an object formed directly with a microwave imaging system is a deformed version of the 2-D plan view of the object.

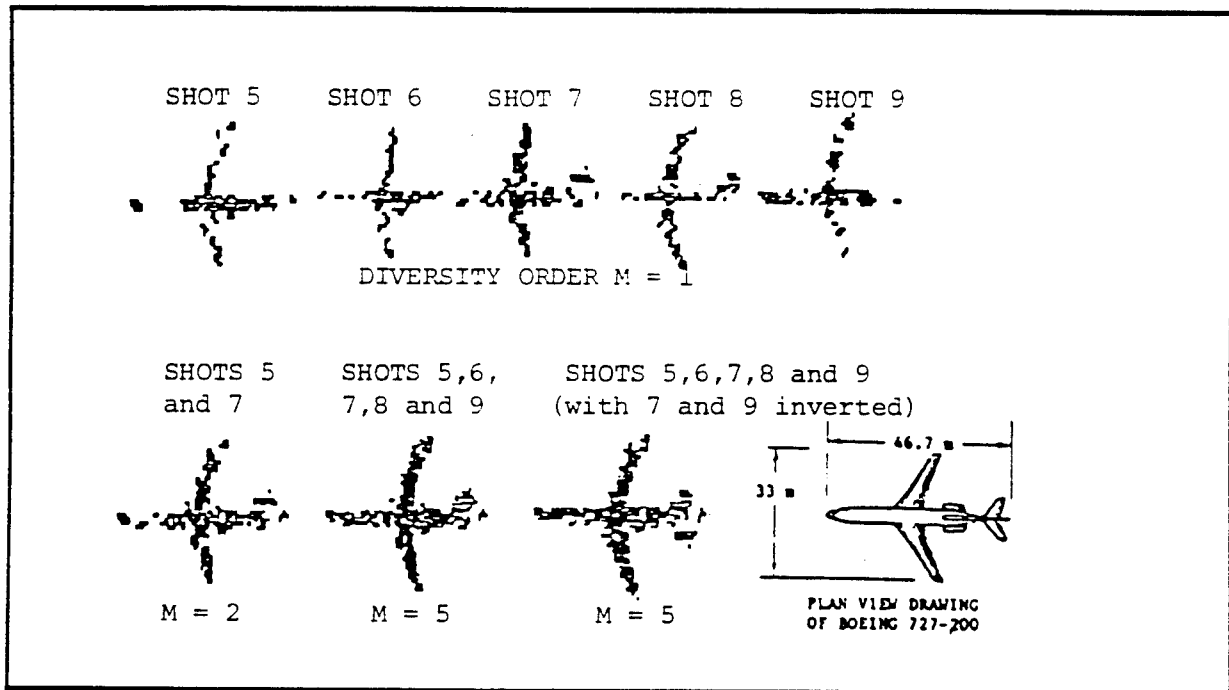


Figure 24 Diversity process exercised on several images of BOEING 727, showing reduced fragmentation

It is important for us to resolve the problem of automatic recognition with limited, incomplete, distorted, or noise-corrupted images. This is especially true when the images are not useful for reliable human identification.

Human nervous systems are well known to be good at recognition from partial, distorted and obscured information: They are able to recall an item from memory easily with only partial information on that item (associative or content-addressable memory.) Artificial neural networks mimic human nervous systems based on neurophysiological and neuroanatomical studies: These networks have many of the attractive features of the human nervous system such as rapid processing, robustness, fault tolerance, capabilities to adapt and continue learning, and they can perform many intelligent information-processing functions

So far, many neural network models have been developed and successfully applied to image recognition. Our preliminary investigations also demonstrate that the recognition of poor microwave imagery based on neural network models is feasible and efficient.

The neocognitron was fashioned by analogy to visual systems, and therefore it could be applied directly to the recognition of low quality 2-D microwave images. In the case of airplanes, the prominent features include the wingspan, the length and width of the fuselage, the locations and numbers of engines, the orientation of the wings with respect to the fuselage, and the shapes and positions of the wings and tail structure.

One of the proposed efforts is to make a detailed comparison of the above three types of neural network models and their relative applicability to the recognition of microwave images. The most suitable model of the three types will then be selected, and improved if necessary.

HARDWARE IMPLEMENTATION OF THE NEURAL NETWORK MODEL

There are three ways to make practical implementations of neural networks: (1) Develop simulation software designed on a general-purpose digital computer to perform the actions of a true neural network; (2) build a special-purpose digital neural network emulator that connects to a general-purpose host system; or (3) construct a true electronic or optical neural network. We plan to build a special-purpose digital hardware emulator to realize our neural network model because the emulator is effective, low in cost and easier to implement.

For this purpose, some advanced digital signal processing microprocessors, such as the ADSP21000 (Analog Devices, Inc.), DSP32C (AT&T Bell Lab.), DPS96002 (Motorola, Inc.), and TMS320C30 (Texas Instruments, Inc.), will be considered. They have many of the characteristics needed by a neural network emulator. For example, the TMS320C30 has a very high speed (60 ns cycle-time). Its very efficient pipeline function can execute each instruction in a single cycle. Its floating-point arithmetic capability permits the handling of numbers of very high dynamic range. Its parallel (single cycle) multiplier instructions and block-repeat capability will be very useful in the implementation of the neural network emulator. In addition, it has one 4K x 32 bits ROM block and two 1K x 32 bits RAM blocks. The separate program buses, data buses, and DMA buses allow for parallel program fetches, data reads and writes, and DMA operations. Because of the on-chip DMA controller, the TMS320C30 can interface to slow external memories and peripherals without reducing throughput to the CPU. In multilayer neural networks, each layer can use a chip to implement its actions. Using this type of microprocessor, we will develop an advanced neural network emulator to implement the automatic recognition of images from microwave imaging systems.

RESULT OF PRELIMINARY INVESTIGATIONS

We used simulated data sets and an experimental data base of high resolution microwave images of commercial aircraft (Boeing 727, Boeing 747, L-1011 and DC-8) flying into Philadelphia International Airport. The radar operated at X-band ($\lambda=3$ cm) with 150 MHz bandwidth. The

resolution cell was approximately 1 m^2 . The target distances from the Valley Forge radio camera are approximately 3 km.

We tested the Hamming net and the multilayer perceptron in our investigations. The airplane images were composed of 59×70 pixels. When the Hamming net was used, the images were first transformed to binary format. Their exemplars were plan-view drawings obtained from an airplane manual. The inputs were fragmented microwave images to which noise has been added. Fig. 25 shows typical results. The first line in Fig. 25 shows the fragmented images without noise and the second line shows them after noise has been added. Noise was added by randomly changing white pixels to black and black pixels to white with a 0.3 probability. This is equivalent to a SNR of 3.7 dB. The third line shows the exemplars chosen by the Hamming network that best match the noisy and fragmented aircraft images. In each case the selection was the correct choice out of four. Experiments consistently demonstrated that the Hamming net can work well if the input imagery is identical in size, position and orientation to its exemplar. If the input images have minor changes in size, position and orientation, the net still can recognize them correctly. When these changes are large, however, mistakes result. The effects of variations in the scale, position and orientation is an important matter to be studied.

Unlike the Hamming net, the Perceptron requires training. When the three-layer perceptron with a rotation-independent net was used, the training set used in the experiment had 20 images of these commercial aircraft. These included two real images produced in the Valley Forge Research Center and three simulated images of each type. The simulated training images were pieces of the exemplars, with up to 50% random fragmentation. The neural network was trained using the backpropagation learning algorithm [14]. Internal thresholds were set to equal 0. During the training process the weight values were changed to improve performance. The trained network was then presented with eight highly fragmented (but noise free) test images excluded from the training data sets. Fig. 26 shows the eight test images. The first line in Fig. 26 shows four real images and the second line shows four simulated images. The test results showed that this network has good ability to generalize, since each of the test images was successfully detected and recognized. The three-layer perceptron with a rotation-independent net can learn to recognize imagery in the training data set, and the trained network could be used to correctly recognize imagery in the test data set.

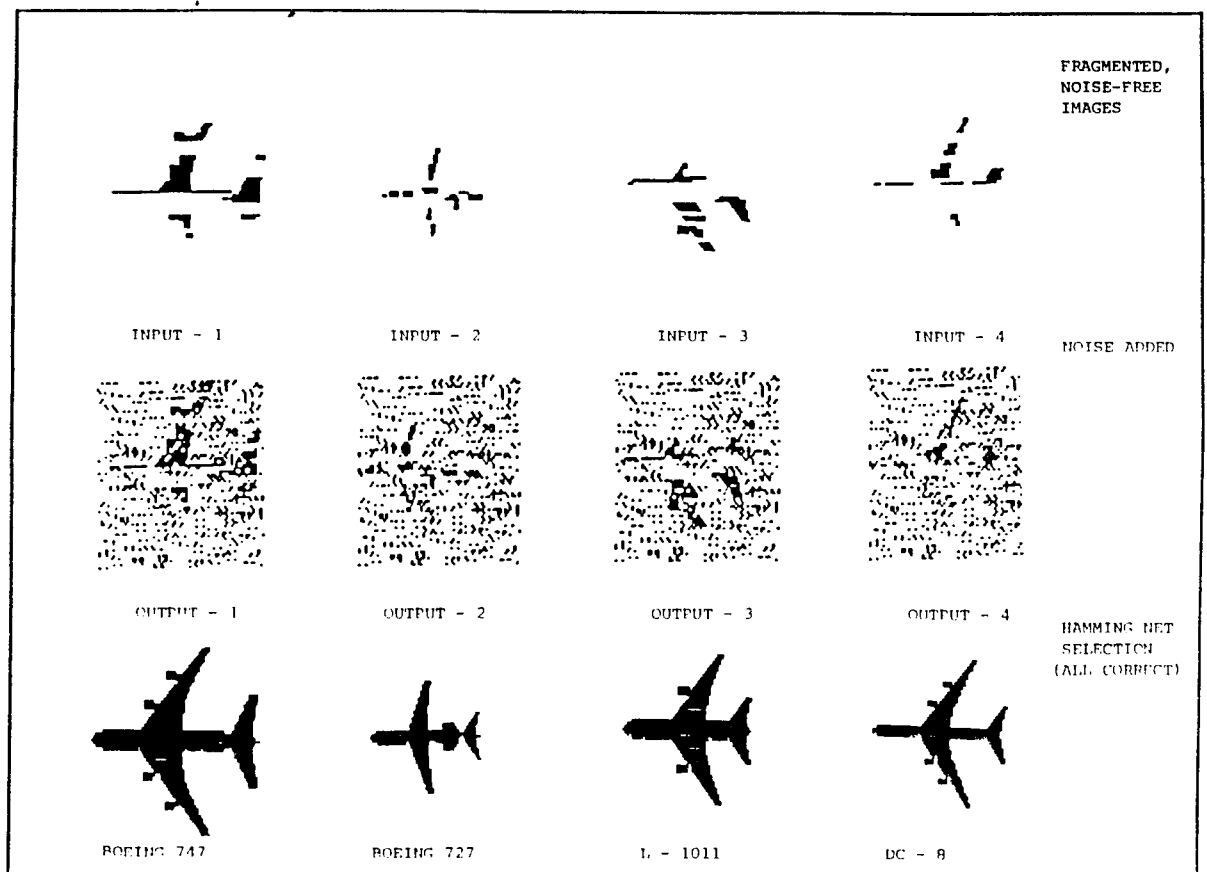


FIGURE 2.5 CORRECT RECOGNITION OF FRAGMENTED, NOISY IMAGES BY HAMMING NETWORK.

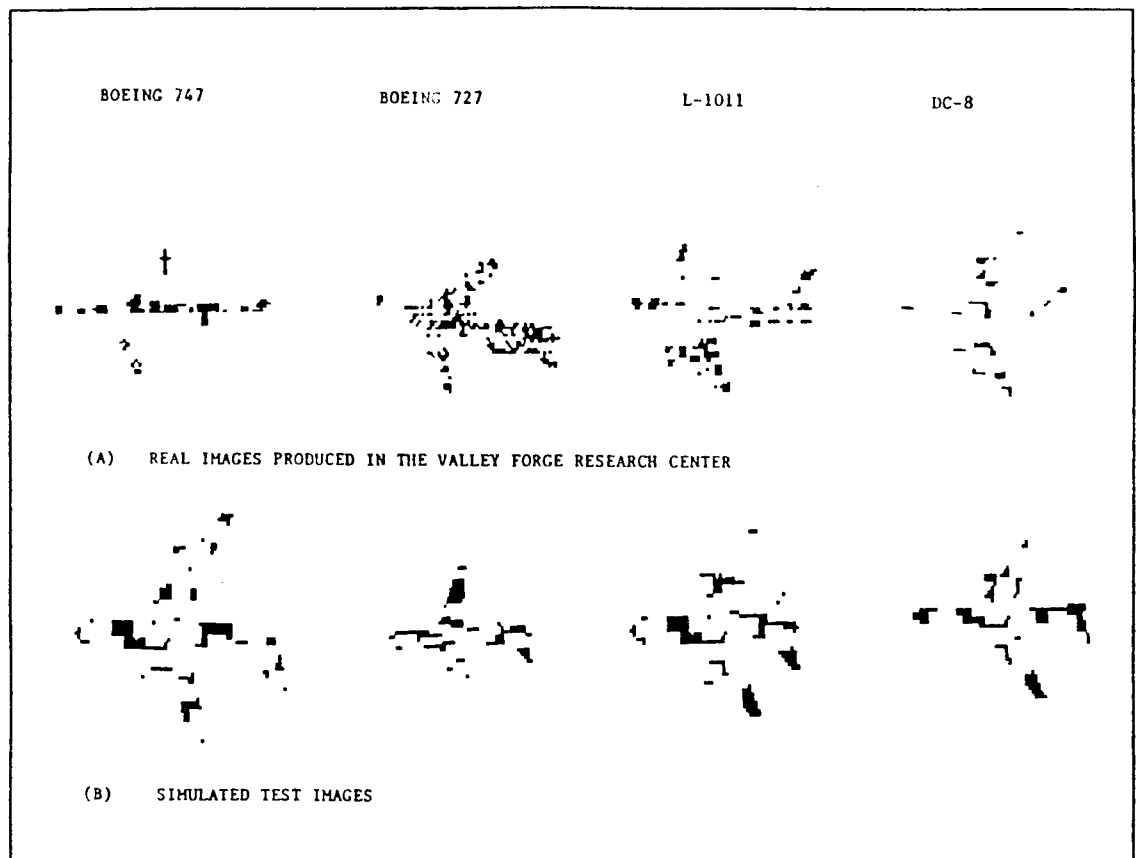


FIGURE 2.6 REAL AND SIMULATED TEST IMAGES.

REFERENCES:

- [1] B.D. Steinberg and H.M. Subbaram. Microwave Imaging Techniques. John Wiley & Sons. 1991.
- [2] J.P. Hamaker, J.D. O'Sullivan, and J.E. Noordam. "Image Sharpness, Fourier Optics, and Redundant-Spacing Interferometry." J. Optical Society of America. Vol. 67, No. 8. August 1977.
- [3] H.M. Subbaram and B.D. Steinberg. "Scene Independent Self-Calibration of Phased Array Antennas." accepted for publication by IEEE Transactions on Antennas and Propagation.
- [4] B. Kang. "Research on Self-Calibrating Algorithms for High-Resolution Microwave Imaging Systems." Ph.D. Dissertation. Dept. of Electrical and Computer Science Engineering, Drexel University, Philadelphia, PA. 1989.
- [5] E.H. Attia and B.D. Steinberg. "Self-Cohering Large Antenna Arrays Using the Spatial Correlation Properties of Radar Clutter." IEEE Transactions on Antennas and Propagation. January. 1989.
- [6] G. Borsari. "The Source Statistics Algorithm." Valley Forge Research Center Progress Report #61. Moore School of Electrical Engineering, University of Pennsylvania, Philadelphia, PA. March 1991.
- [7] J. Tsao. "Phased Array Beamforming by Parseval's Theorem." IEEE SP-S International Symposium. PA. June 1986.
- [8] B.D. Steinberg. Microwave Imaging With Large Antenna Arrays. John Wiley & Sons. New York. 1983.
- [9] T. Ozdemir, S. Roy, and R.S. Berkowitz. "A Bistatic System for Imaging of Shallow Subsurface Objects." to be published in IEEE Transactions on Geoscience and Remote Sensing.
- [10] OSD/DARPA Ultra-Wideband Radar Review Panel. "Assesment of Ultra-Wideband (UWB) Technology." DARPA, Arlington, VA. July 1990.
- [11] B.D. Steinberg and B. Kang. "Radar Detection Sensitivity as a Function of Target Dimensionality." Valley Forge Research Center Quarterly Progress Report No. 58. pp. 20-22. September 1989.
- [12] B.D. Steinberg and B. Kang. "Experiments With Stereo Display." Valley Forge Research Center Quarterly Progress Report No. 57. pp. 62-64. March 1989.
- [13] C.W. Tyler. "Spatial Limitations of Human Stereoscopic Vision." Three Dimensional Imaging. S.A. Benton, Editor. Proc. SPIE 120. pp. 36-42. 1977.
- [14] Rumelhart, D.E., Hinton, G.E., and Williams, R.J.. "Learning Internal Representations by Error Propagation." Parallel Distributed Processing. vol. 1. pp. 318-362. MIT Press. 1986.